1

2

Large pilin subunits provide distinct structural and mechanical properties for the *Myxococcus xanthus* type IV pilus

Anke Treuner-Lange[1,*], Weili Zheng[2,#], Albertus Viljoen[3], Steffi Lindow[1], Marco Herfurth[1], Yves F. Dufrêne[3], Lotte Søgaard-Andersen[1] and Edward H. Egelman[2,*]

[1] Max Planck Institute for Terrestrial Microbiology, 35043 Marburg, Germany

[2] Department of Biochemistry and Molecular Genetics, University of Virginia School of Medicine, Charlottesville, VA 22903, USA

[3] Louvain Institute of Biomolecular Science and Technology, UCLouvain, B-1348 Louvain-la-Neuve, Belgium

[#] Present address: Nanoimaging Services, San Diego, CA 92121, USA

[*] Corresponding authors: anke.treunerlange@mpi-marburg.mpg.de, egelman@virginia.edu

16

17

1

Summary

Type IV pili (T4P) are ubiquitous bacterial cell surface filaments important for surface motility, adhesion to biotic and abiotic surfaces, DNA uptake, biofilm formation, and virulence. T4P are built from thousands of copies of the major pilin subunit and tipped by a complex composed of minor pilins and in some systems also the PilY1 adhesin. While the major pilins of structurally characterized T4P have lengths of up to 161 residues, the major pilin PilA of *Myxococcus xanthus* is unusually large with 208 residues. All major pilins have a highly conserved N-terminal domain and a highly variable C-terminal domain, and the additional residues in the *M. xanthus* PilA are due to a larger C-terminal domain. We solved the structure of the *M. xanthus* T4P (T4P^{Mx}) at a resolution of 3.0 Å using cryo-electron microscopy (cryo-EM). The T4P^{Mx} follows the structural blueprint observed in other T4P with the pilus core comprised of the extensively interacting N-terminal α1-helices while the globular domains decorate the T4P surface. The atomic model of PilA built into this map shows that the large C-terminal domain has much more extensive intersubunit contacts than major pilins in other T4P. As expected from these greater contacts, the bending and axial stiffness of the T4P^{Mx} is significantly higher than that of other T4P and supports T4P-dependent motility on surfaces of different stiffnesses. Notably, T4P^{Mx} variants with interrupted intersubunit interfaces had decreased bending stiffness and strongly reduced motility on all surfaces. These observations support an evolutionary scenario whereby the large major pilin enables the formation of a rigid T4P that expands the environmental conditions in which the T4P system functions.

Introduction

Bacterial motility is important for virulence, colonization of various habitats, biofilm formation, interactions with host cells, and fitness by directing cells toward nutrients and away from toxins and predators[1]. Accordingly, bacteria can move in many different environments and their motility devices are adapted to these varying conditions[1,2]. Generally, bacteria move using highly conserved nanomachines that energize either the rotation of flagella to enable swimming in liquids and swarming on semisolid surfaces or the extension/retraction of type IV pili (T4P) to enable translocation on solid surfaces[1,2]. Some bacteria also move on surfaces by gliding, but the involved nanomachines are more diverse, each with a narrow taxonomic distribution[1,2]. Here, we focus on T4P, which are not only important for motility but also for adhesion to host cells and abiotic surfaces, natural transformation with horizontal gene transfer, biofilm formation, virulence, predation, and surface sensing[3,4].

The versatility of T4P depends on their ability to undergo cycles of extension with adhesion to a surface, and retractions that generate a force sufficient to pull a cell forward[5-8]. These cycles are driven by the T4P machine (T4PM), which is composed of ~15 conserved proteins forming a large macromolecular complex that spans from the outer membrane across the periplasm and inner membrane (IM) to the cytoplasm[9-11]. T4P extension and retraction are powered by the ATPases PilB and PilT, respectively that bind to the cytoplasmic base of the T4PM in a mutually exclusive manner[3,10,12]. All ~15 proteins are essential for T4P extension except for PilT, which is only necessary for retraction[3]. The T4P are flexible, thin, up to several microns in length, and composed of thousands of copies of the major pilin subunit as well as a tip complex comprising minor pilins and sometimes also the PilY1 adhesin[11,13-16]. During T4P extension, major pilin subunits are extracted from a reservoir in the IM and inserted at the base of the growing pilus; during T4P retractions, this process is reversed, and the major pilin subunits are removed from the base of the T4P and reinserted into the IM[3].

Major pilins are synthesized as prepilins with an N-terminal type III signal peptide (T3SP), which is cleaved off by the PilD prepilin peptidase between the Gly and Phe residues in the consensus GFxxxE motif to generate the mature major pilin (hereafter simply referred to as the major pilin)[17]. Sequence and structural analyses of major pilins in isolation and structural studies of intact T4P filaments have shown that major pilins share the same overall structure with a semi-conserved N-terminal α-helix (α1) and a highly variable C-terminal, largely β-stranded, globular domain[4,13]. In Gram-positive bacteria, the C-terminal domain can be all α-helical[18], while in *Geobacter sulfurreducens* it has now been shown that the two domains are

3

72   encoded by two different genes[19], resulting in a pilin subunit containing two polypeptide chains.

73   Proteins homologous to major pilins are also the building blocks of the endopilus (previously

74   called pseudopilus) of the type II secretion system as well as archaeal T4P and flagella[4]. Since

75   in archaea both T4P pilins and flagellins have homology with only the N-terminal bacterial pilin

76   domain, the suggestion has been made that all pilins have arisen from a gene fusion of

77   ancestral genes encoding the N- and C-terminal domains separately[20]. The α1-helix can be

78   divided into the mainly hydrophobic highly-conserved N-terminal part (α1-N), which is essential

79   for anchoring the pilin in the IM before its incorporation into the pilus, and the less conserved

80   amphipathic C-terminal part (α1-C) that connects to and packs against the globular C-terminal

81   domain[4,13].

82   The structures of eight bacterial T4P filaments, including an endopilus of a type II

83   secretion system, have been solved to a resolution of 3.2-8.0 Å, from *Neisseria gonorrhoeae*

84   (PDB 5VXX)[21], *N. meningitidis* (PDB 5KUA)[22], *Pseudomonas aeruginosa* (PDB 5VXY)[21],

85   *Escherichia coli* (PDB 6GV9)[23], *G. sulfurreducens* (PDB 6VK9 and 7TGG)[19,24], *Klebsiella*

86   *oxytoca* (PDB 5WDA; endopilus)[25] and two different ones from *Thermus thermophilus* (PDB

87   6XXD and 6XXE)[26]. These structures revealed, not surprisingly, that all T4P filaments share the

88   same overall architecture. Specifically, the major pilins are helically arranged and tightly packed,

89   giving rise to pili with widths of ~60-75 Å, a rise of ~9-11 Å per subunit, and ~4 subunits per

90   turn, with ~1000 subunits per micron length of the T4P. The pilus core comprises the

91   extensively interacting α1-helices while the variable globular domains decorate the T4P surface.

92   In this conserved structural blueprint, the α1-helices establish the backbone of the T4P, while

93   the divergent globular domains determine the shape, surface charge, and functional properties

94   of T4P[21-23,25-27]. While the C-terminal globular domain remains largely unchanged upon the

95   incorporation of a major pilin into the pilus, the α1-helix undergoes a partial loss of α-helical

96   structure of variable length around the highly conserved Pro22 residue[19,21,22,26]. It was

97   suggested that the melting of this segment is essential for the tight packing of the major pilins[21].

98   The extensive interactions between major pilins make T4P highly robust, and in the case of *N.*

99   *gonorrhoeae* and *M. xanthus,* T4P were shown to withstand pulling forces of 110 to 150pN,

100   respectively, during retractions[7,8]. In addition, T4P of *N. gonorrhoeae, N. meningitidis* and *P.*

101   *aeruginosa* have been shown to be highly extensible, undergoing force-induced conformational

102   changes to elongate in response to pulling forces[28-31]. Moreover, in *N. gonorrhoeae,* these

103   conformational changes were shown to be reversible[29]. Whether this resilience is a conserved

104   feature of T4P is not known. It was proposed[21] that further melting of the N-terminal α-helix is

105 responsible for the extensibility of these filaments, and the restoring force after extension would

106 be provided by the refolding of the α-helix.

107 Major pilins are not only diverse in sequence but also in size[4]. Among the solved T4P

108 structures, the major pilins vary in size from 111-161 residues[21-23,26], while the two polypeptide

109 chains forming the *G. sulfurreducens* pilin have a combined size of 165 residues[19,24]. *M. xanthus*

110 is a model system for understanding the architecture and mechanism of the T4PM[10,11]. Of note,

111 the major pilin PilA of *M. xanthus* contains 208 residues[32] and is, thus, significantly larger than

112 those of solved T4P structures. Moreover, the *M. xanthus* T4P (henceforth T4P[Mx]) is highly

113 robust and can withstand a pulling force of 150pN during retractions[7]. *M. xanthus* is a predatory

114 soil bacterium and belongs to the myxobacteria, prolific secondary metabolite producers[33]. *M.*

115 *xanthus* has a biphasic nutrient-regulated lifestyle in which cells organize to form spreading,

116 predatory colonies in the presence of nutrients and spore-filled fruiting bodies in the absence of

117 nutrients[34,35]. In both phases of the lifestyle, motility has a key function. *M. xanthus* has two

118 motility systems for translocation across surfaces, one for gliding and one that depends on

119 T4P[34,35]. These two motility systems enable *M. xanthus* cells to translocate on highly diverse

120 surfaces[36].

121 To understand the properties conferred by large major pilins to T4P filaments, we

122 determined the structure of T4P[Mx] using cryo-EM to a resolution of 3.0 Å, which allowed us to

123 build *de novo* an atomic model of the entire major pilin, and analyzed its biophysical properties

124 *in vitro.* This structure revealed a T4P that differed from all existing T4P structures since it had

125 much more extensive contacts between the globular domains. Consistent with such a structure,

126 the stiffness of T4P[Mx] is significantly higher than that of *N. gonorrhoeae* and *P. aeruginosa* T4P.

127 Structure-guided mutagenesis of PilA showed that disruption of subunit interfaces caused a

128 reduction in the axial stiffness of the T4P, and these variant T4P were less efficient in

129 supporting motility on surfaces of different stiffness.

130

Results

Major pilins vary significantly in size

131
132
133 To systematically assess the size of major pilins, we first extracted all sequences of the
134 K02650 group (type IV pilus assembly protein PilA) from the KEGG Orthology (KO) database[37].
135 After filtering out sequences with >90% sequence identity, sequences lacking a T3SP, and/or
136 sequences lacking a classified taxonomy, we obtained a set of 1,955 prepilins of T4P. After
137 removal of the T3SP, the major pilins vary in length from 42 to 297 aa, with a mean of 141±25
138 aa, in good agreement with a previous estimate based on fewer sequences[13] (Fig. 1A, Table
139 S1). Because the largest structurally characterized major pilin has a size of 161 aa (and 165 aa
140 for the heterodimeric *G. sulfurreducens* major pilin), we arbitrarily defined large major pilins as
141 proteins with a size ≥166 aa. Among our set of 1,955 sequences, 226 proteins, representing
142 12%, fulfilled this criterion. These proteins are widespread and present in 13 of the 21 phyla with
143 major pilins, and largely group according to phylogeny (Fig. 1A; Fig. S1; Table S1). However,
144 their distribution in phyla and classes is highly skewed, and at the phyla and class levels, they
145 are overrepresented in Betaproteobacteria (20%), Cyanobacteria (23%), Myxococcota (93%)
146 and Bdellovibrionota (100%) (Fig. 1A, Table S1). Moreover, while the length distribution of major
147 pilins in Betaproteobacteria (42-279 aa) and Cyanobacteria (105-243 aa) is broad (Fig. 1A), it is
148 more narrow in the predatory Myxococcota (153-217 aa) and Bdellovibrionota (170-204 aa)
149 (Fig. 1A). Interestingly, in the Betaproteobacteria, the large major pilins are enriched explicitly in
150 the order Burkholderiales (66 of 75) (Table S2), an ecologically diverse order that includes plant,
151 animal and human pathogens[38], and especially in the *B. cepacia* complex, which is associated
152 with cystic fibrosis[39,40]. Similarly, in the Firmicutes, the large mature major pilins are highly
153 enriched in the order Eubacteriales (19 of 25), which includes several species of the gut
154 microbiome (Table S2) in which T4P are ubiquitous[41,42].

155 To understand the size variation among the mature major pilins, we performed sequence
156 analyses and secondary structure predictions based on a multiple sequence alignment of the
157 1,955 major pilins and the major pilins of previously solved T4P structures (Fig. 1B, C). The
158 secondary structure consensus revealed an N-terminal α1-helix with an average length of 51 aa
159 (Fig. 1B), in agreement with a previous study[4]. The amino acid consensus revealed that the N-
160 terminal portion is predominantly hydrophobic and more highly conserved than the C-terminal
161 portion of the α1-helix. The N-terminal portion of α1-helix is inserted in the IM before pilus
162 assembly, which accounts for the hydrophobicity. Comparison of these two regions to the major
163 pilins of solved T4P structures shows that they correspond well to the hydrophobic α1-N and the

6

164   amphipathic α1-C (Fig. 1B, C). Thus, the size difference among major pilins arises from size

165   differences in the globular domain.

166   *Cryo-EM structure of the M. xanthus T4P reveals unusual packing*

167   To understand the properties of T4P built from a large major pilin, we focused on T4P[Mx].

168   The mature PilA (MXAN_5783) has a length of 208 aa with a predicted α1-N highly similar in

169   sequence to the major pilins of the solved T4P structures, but with the predicted amphipathic

170   α1-C containing more basic and less hydrophobic residues than those other major pilins (Fig.

171   1B). For structure determination of T4P[Mx], we purified T4P from the hyper-piliated Δ*pilT* strain, in

172   which T4P are extended but not retracted (Fig. 2A, S2A, B). We used cryo-EM to determine the

173   structure of the T4P[Mx] and obtained the structure at 3.0 Å resolution, the highest resolution so

174   far reported for a T4P structure (Fig. 2B, S2C).

175   The subunits in the filament are related to each other by an azimuthal rotation of 100.7°

176   and an axial rise per subunit of 10.0 Å, generating a right-handed 1-start helix with a pitch of

177   ~36 Å and 3.6 subunits per turn. The filaments are ~7 nm in diameter and, in contrast to all

178   previous T4P structures, resemble a rather solid cylinder without the modulation of the surface

179   due to smaller C-terminal domains (Fig. 2C, S3A). The individual PilA subunits within the cryo-

180   EM reconstruction follow the overall blueprint of major pilins in solved T4P structures with the N-

181   terminal α1 generating the core of the pilus and the globular C-terminal domain decorating the

182   surface (Fig. 2D). We also note that the solved structure of the T4P[Mx] with its diameter of ~7 nm

183   readily fits into the overall architecture of the *M. xanthus* T4PM, which we previously solved

184   using cryo-electron tomography[10] (Fig. 2E).

185   The 3.0 Å-resolution of the T4P[Mx] structure allowed for building *de novo* an atomic model

186   of individual PilA subunits (Fig. 2D, Fig. 3A). The N-terminal α1-helix of PilA[Mx] extends from

187   residues 3-54 and contains the hydrophobic α1-N (aa 3-18) and the amphipathic α1-C (aa 24-

188   54) separated by an unfolded stretch of five residues around the conserved P22 (Fig. 1B, 2D,

189   3A, B, S3B). This is similar to the local melting of this helix seen in major pilins in previous T4P

190   structures[20] (Fig. 1C, S3B).

191   The large globular domain (aa 55-208) contains two antiparallel β-sheets, one four-

192   stranded sheet composed of β1-4 and one three-stranded sheet composed of β1'-3', as well as

193   three α-helices (α2-4) (Fig. 3A, B). These regular structural elements (α-helices, β-strands),

194   which are interrupted by loops, account for ~26% of the globular domain (Fig. S3B). Compared

195   to the major pilins of the other solved structures, the extra residues in PilA[Mx] are largely found in

196 a region between β1 and α3 and a region forming β3, β2' and β3' (Fig. S3C), and while those

197 previous structures all have a contiguous antiparallel four-stranded β-sheet[19,21-23,25-27], the two

198 antiparallel β-sheets in PilA^{Mx} are non-contiguous (Fig. 3A, B, S3B, C).

199 Two disulfide bridges are present in the large globular domain. C95/C102 connects and

200 likely stabilizes the region between β1 and α3. C183/C203 connects the β'-sheet to the C-

201 terminal part of the globular domain (Fig. 3A, B), somewhat similar to the C-terminal D-region

202 known from other pilins that attaches the β-sheet to the C-terminal portion of the globular

203 domain[4].

The large globular domain is involved in extensive intersubunit interactions

205 Within the T4P^{Mx} the globular domain of an individual PilA monomer extensively interacts

206 with neighboring subunits (Fig. 3C), including six different subunit-subunit interfaces, three large

207 (N:N-3, N:N-4, N:N-1) and three small (N:N-7, N:N-2, N:N-6) (Fig. 3C, D). In total, these

208 interfaces add up to ~ 3000 Å^2 of buried surface area (Fig. 3D). Because a pilin subunit interacts

209 with pilins above and below, every individual pilin subunit has a total of 12 interaction partners,

210 adding up to a total of ~6000 Å^2 of buried surface area per pilin.

211 The structure of the wide T4P of *T. thermophilus (*T4P^{Tt-w}*)* composed of the 125 aa PilA4

212 pilin was also solved at a high resolution (Fig. S3A)[26], allowing a direct comparison of subunit

213 interface areas between the T4P^{Mx} and T4P^{Tt-w}. T4P^{Tt-w} also has six subunit interfaces and

214 similarly to the T4P^{Mx}, the largest interfaces occur between N:N-3, N:N-4 and N:N-1 (Fig. 3D). In

215 comparison to the T4P^{Tt-w}*,* there is a ~50% increase in the buried interfacial area per subunit in

216 the T4P^{Mx} (Fig. 3D), deriving largely from more extensive interactions in the N:N-3 and N:N-1

217 interfaces. Similarly, a comparison of the N:N-3, N:N-4, and N:N-1 interfaces of T4P^{Mx} with

218 those of the lower resolution T4P structures of the *E. coli* EHEC (major pilin, 140aa), *N.*

219 *gonorrhoeae* (major pilin, 158aa), *N. meningitidis* (major pilin, 161aa), and *P. aeruginosa* PAK

220 (major pilin, 143aa) shows that these three interfaces in these four structures vary from ~1500-

221 2000 Å^2 [23], and are thus also significantly smaller than in the T4P^{Mx}.

A structural model of the complete T4P^{Mx} including the tip complex

223 *M. xanthus* encodes three sets of each four minor pilins and one PilY1 adhesin[11,14,15]. At

224 least two of these three sets, i.e. those encoded by gene cluster_1 and gene cluster_3, not only

225 form a priming complex for pilus assembly but also a tip complex involved in adhesion[11,14,15].

226 Similar to major pilins, minor pilins are composed of an N-terminal α1-helix and a globular C-

8

227   terminal domain[4]; PilY1 proteins share a conserved C-terminal domain while the N-terminal

228   domain is more variable[43].

229   For the complex formed by the cluster_3 proteins, it was proposed that the less conserved N-

230   terminal domain of PilY1.3 sits at the top while the conserved C-terminal domain interacts with a

231   complex composed of four minor pilins below, which, in turn, interact with PilA below[11].

232   Specifically, based on pull-down experiments and direct interaction analyses, the minor pilin

233   PilX3 was placed directly below PilY1.3, followed by PilW3, FimU3, PilV3 and PilA [11]. To

234   generate the first complete structural model of a T4P, we first generated a structural model

235   using AlphaFold-Multimer of the tip complex composed of one copy each of the major pilin, the

236   four minor pilins and PilY1 using the proteins of cluster_3[11].

237   A high confidence AlphaFold-Multimer model (Fig. S2D), largely confirmed the suggested

238   organization of this complex with PilY1.3 at the top followed by PilX3, PilV3, PilW3, FimU3 and

239   PilA at the base, i.e. the only difference is the placement of PilV3 between PilW3 and PilX3 (Fig.

240   S2E). In the AlphaFold-Multimer model only α1 of PilA is slightly kinked (around the conserved

241   P22) (Fig. S2E), while the four minor pilins lack that residue[11]. Interestingly, a stretch of eight

242   amino acids residues of the C-terminal end of PilY1.3 is modeled to form a β-strand, which,

243   together with two β-strands of PilX3, forms an three-stranded antiparallel β-sheet (Fig. S2F),

244   suggesting that PilX3 and PilY1.3 interact by β-strand addition, more precisely by β-sheet

245   augmentation[44]. Interestingly, despite substantial sequence diversity between cluster_3 and

246   cluster_1 components[11,14], the same order of components as well as the proposed β-sheet

247   augmentation between PilX1 and PilY1.1 is predicted for the high confidence AlphaFold-

248   Multimer model of the cluster_1 proteins (Fig. S2G, H, I). Protein-protein interactions by β-

249   strand addition are also involved in the assembly and stabilization of the Type 1 pilus[45], and are

250   reported to be extraordinarily stable against dissociation and unfolding[46]. To generate the

251   complete model of the T4P^Mx including the tip complex, we fitted the model of the tip complex of

252   the cluster_3 proteins into the T4P^Mx structure by superposing the top PilA of the T4P^Mx with the

253   PilA of the AlphaFold-Multimer model (Fig. 2F). Importantly, these two PilA molecules could

254   readily be superposed giving rise to a structure in which the four minor pilins tops the T4P^Mx

255   followed by the PilY1.3 adhesin firmly attached through its C-terminal domain to PilX3 via β-

256   sheet augmentation.

257

258   *T4P^Mx has increased bending and axial stiffness compared to less compact T4P*

259   Since the resistance to bending will scale as the fourth power of the radial mass
260   distribution, we expected that the increased contacts between the outer domains near the
261   outside of the pilus would make the T4P[Mx] filament more rigid than previously studied ones. We
262   quantified its bending stiffness with the persistence length (PL). Because the persistence length
263   is derived from an analysis of fluctuations in curvature from filaments at thermodynamic
264   equilibrium, cryo-EM is ill-suited for making such measurements, due to the large forces present
265   from both fluid flow during blotting and the compression of long filaments into a thin film[47,48].
266   Consequently, we used purified T4P[Mx] visualized by negative stain transmission electron
267   microscopy (TEM) and determined a PL of 21μm for T4P[Mx] (Fig. S3A, S4A). In parallel
268   experiments, we determined the PL of the less compact T4P of *N. gonorrhoeae* (major pilin,
269   158aa; Fig. S3A) and *P. aeruginosa* PAK (major pilin, 144aa; Fig. S3A) as 11μm and 13μm,
270   respectively (Fig. S3A, S4A). We conclude that the more extensive C-terminal domain contacts
271   in the T4P[Mx] do indeed result in increased bending stiffness.

272   We also expected that these increased contacts would reduce the axial compliance,
273   resulting in a greater force needed to extend these filaments. We therefore analyzed the force-
274   extension behaviour and adhesive properties of T4P[Mx] in live cells using atomic force
275   microscopy (AFM) force spectroscopy (FS) as described for T4P in *P. aeruginosa* PAO1 and
276   PA14 (major pilin length:143 & 173 aa, respectively)[28,30,49]. Those studies reported two distinct
277   force-extension profiles when single T4P on live cells were pulled: (i) a tensile force that initially
278   increased in an approximately linear fashion with pilus stretching before rupturing of the contact
279   between the pilus and the AFM tip; and (ii) an initial increase in force followed by a constant
280   force plateau before rupture occurred. Because of the approximate linearity of the first type,
281   these profiles were called linear nanosprings, and their spring constant k_{pilus}, which is a measure
282   of pilus axial stiffness, was quantified as ~2 pN/nm[28,30]. We applied the AFM-FS methodology
283   used in[30] to characterize T4P[Mx] on live cells (Methods). Briefly, we covalently modified a gold
284   AFM tip to make it hydrophobic. Subsequently, single *M. xanthus* cells adhering to a polystyrene
285   surface were visualized with an inverted microscope and force probed in buffer with the
286   hydrophobic AFM tip. Specifically, because T4P[Mx] are localized to one of the cell poles[50], the
287   AFM probe, initially at a specified height above the sample, is displaced downwards close to a
288   piliated cell pole until a T4P, which is freely moving in the buffer, by chance adheres via
289   hydrophobic interactions to the AFM tip (Fig. 4A, i). Then the probe is moved upwards at a
290   constant velocity, thereby also lifting the relaxed pilus (Fig. 4A, ii) until it reaches its initial height
291   (Fig. 4A, iii). During this movement, a bound T4P is loaded with tension causing its extension
292   and resulting in the downward bending of the cantilever, thereby allowing the quantification of

10

293 the tensile force (Fig. 4A, iii). Once the tensile force exceeds the strength of the interactions

294 between the pilus and the AFM tip, the contact between the pilus and the AFM tip ruptures and

295 the cantilever relaxes (Fig. 4A, iv). The T4P extension until rupture of the pilus-AFM tip contact

296 is recorded as force-distance (*F-d*) curves (Fig. 4A). From such *F-d* curves over a raster grid in

297 force volume mode (Methods), we constructed correlated topographic and adhesion maps,

298 thereby pinpointing the exact location of pilus signatures (Fig. S4B). As previously observed for

299 *P. aeruginosa* T4P, we observed both nanospring (Fig. 4B) and force plateau signatures (Fig.

300 S4C) almost exclusively close to one of the cell poles for wild-type (WT) *M. xanthus* cells. By

301 contrast, such signatures were nearly absent in *M. xanthus* Δ*pilA* cells (Fig. S4D). The

302 measured rupture forces in the pilus nanosprings (~120pN) (Fig. 4C) and force plateaus

303 (~220pN) (Fig. S4C) were similar to those reported for *P. aeruginosa* T4P[28,30,49], indicating no

304 differences in the adhesive properties between *M. xanthus* and *P. aeruginosa* pili. The spring

305 constant k_{pilus} of T4P[Mx] at low (1μm/s as in[30]) and at moderate (5μm/s as in[28,49]) pulling speeds

306 was ~4.0pN/nm and ~5.5pN/nm, respectively (Fig. 4C). Importantly, these values are at least

307 two-fold higher than those reported for T4P in *P. aeruginosa* PAO1 and PA14[28,30], indicating a

308 greater average axial stiffness of the T4P[Mx] and that T4P[Mx] are more resistant to stretching than

309 T4P of *P. aeruginosa*.

310   We also note that even though the mean rupture forces in the pilus nanosprings (Fig.

311 4C) and force plateaus (Fig. S4C) were in close agreement with the reported values for *P.

312 aeruginosa* T4P, T4P[Mx] can resist pulling forces up to 400-500 pN before the contact between

313 the pilus and the AFM tip ruptures (Fig. S4C) while T4P of *P. aeruginosa* resisted forces only up

314 to 250 pN[30]. Nevertheless, T4P[Mx] have elastic properties and undergo a force-induced

315 elongation in response to pulling forces as previously described for T4P of *N. gonorrhoeae, N.

316 meningitidis* and *P. aeruginosa*[28-31] consistent with the previous hypothesis that the extensibility

317 arises from further melting of the N-terminal α-helix[21].

Disruption of PilA subunit-subunit interfaces reduce persistence length

319   Among the six interfaces between PilA subunits in the T4P[Mx], N:N-3, N:N-4 and N:N-1

320 are not only the largest contributors to the subunit interface but also significantly more extensive

321 than those in the T4P[Tt-w] (Fig. 3C-D), and the T4P of *E. coli* EHEC, *N. gonorrhoeae*, *N.

322 meningitidis,* and *P. aeruginosa* PAK. To assess how these three interfaces contribute to pilus

323 bending stiffness and to T4P function *in vivo*, we mutagenized charged residues engaged in salt

324 bridge formation in these three interfaces (Fig. 5A-C). Specifically, we targeted the residues

325 R30, K37, E53 at the N:N-3 interface, D55, R73, R109 at the N:N-4 interface, and K48, E69,

11

326 R70 at the N:N-1 interface and substituted these residues separately with residues with either a

327 polar side chain (Asn or Gln) or Ala. These nine residues are either localized in α1-C (R30, K37,

328 K48, E53) or in the globular domain (D55, E69, R70, R73, R109) (Fig. 3B), and are forming salt

329 bridges connecting either α1-helices (R30, K37, E53 at the N:N-3 interface), globular domains

330 (D55, R73, R109 at the N:N-4 interface, R70, E175 at the N:N-1 interface), or α1-helices and

331 globular domains (K48, E69 at the N:N-1) of the corresponding subunits (Fig. 5A-C). The

332 corresponding 18 mutations were introduced into the *pilA* gene at the native locus of the WT

333 and in the retraction-deficient Δ*pilT* mutant to distinguish between T4P extension and hyper-

334 retraction defects caused by these substitutions.

335 We first examined the accumulation of the PilA variants in total cell extracts and their

336 ability to support T4P formation. Substitutions of four of the nine residues (K37, E53 of α1-C and

337 R70, R73 of the globular domain) (Fig. 5A-C) caused strongly reduced or abolished PilA*

338 accumulation in total cell extracts of both strain backgrounds (Fig. 5D, E). Consistently, in a T4P

339 shear-off assay in which pili are sheared off the surface of cells, these PilA variants did not

340 support T4P formation in either strain background (Fig. 5D, E). Thus, these residues are

341 important for PilA stability and lack of T4P formation is neither due to an extension defect nor a

342 hyper-retraction defect.

343 Mutagenesis of the remaining five residues allowed PilA* accumulation in total cell

344 extracts in both strain backgrounds at the same or slightly lower level than PilA^{WT} (Fig. 5D, E).

345 Except for the D55A variant, they supported T4P formation in both strain backgrounds at

346 essentially the same level as PilA^{WT} (Fig. 5D, E). Paradoxically, the D55A variant, while

347 accumulating in both strain backgrounds, only supported T4P formation in the WT but not in the

348 Δ*pilT* mutant. From here on, we focused on the nine variants that accumulated and supported

349 T4P formation in both strain backgrounds.

350 To assess the mechanical properties of the nine variant T4P, we purified them from the

351 Δ*pilT* background and determined their PL (Fig. 5F). All nine variants had a moderately to

352 strongly reduced PL (Fig. 5F, S5). In particular, substitutions in the N:N-4 interface caused

353 dramatic reductions in PL (Fig. 5F), while substitutions in the N:N-3 and N:N-1 interfaces

354 generally only caused a ~50% reduction in PL (Fig. 5F). We conclude that the substitutions do

355 not interfere with the extension of T4P; however, the T4P assembled by the PilA variants have

356 decreased bending stiffness.

357 *Disruption of PilA subunit-subunit interfaces reduces T4P-dependent motility*

12

358   To analyze whether PilA subunit interface disruption affects T4P-dependent motility, we

359   analyzed the *M. xanthus pilT*[+] strains synthesising these nine variants. *M. xanthus* moves by

360   T4P-dependent motility, which is favoured on soft, moist surfaces, and by gliding motility, which

361   is favoured on hard agar[36]. Surface stiffness was reported to stimulate T4P-dependent motility

362   in *P. aeruginosa*[51]. Therefore, we tested WT as well as the strains expressing the nine PilA

363   variants on soft agar of different stiffness by using a range of agar concentrations (0.4-0.7%)

364   and the increase in colony diameter at 24 hrs as a readout for T4P-dependent motility. The

365   Δ*pilA* strain, which only moves by gliding motility, served as a negative control for T4P-

366   dependent motility and to verify that gliding motility did not significantly contribute to the

367   increase in colony diameter under these conditions.

368   The WT displayed T4P-dependent motility on all four agar surfaces generating the

369   characteristic flares at the colony edge, and the colony diameter increased ~2.5-fold with the

370   agar concentration, while the Δ*pilA* mutant, as expected, generated smooth-edged colonies and

371   only displayed a minor increase in colony diameter (Fig. 5G). These findings are consistent with

372   the observation that surface stiffness stimulates T4P-dependent motility in *P. aeruginosa*. All

373   strains expressing a PilA variant had strongly reduced T4P-dependent motility at all agar

374   concentrations (Fig. 5G). Like the WT, they generally showed improved T4P-dependent motility

375   with increasing agar concentrations; however, none reached the WT level even at 0.7% agar

376   (Fig. 5G). We conclude that WT T4P^{Mx} supports T4P-dependent motility on surfaces of different

377   stiffnesses and more efficiently at higher agar concentrations. In contrast, the T4P of the

378   variants are less efficient at supporting motility under all the tested conditions and are only

379   slightly stimulated on stiffer surfaces.

380

Discussion

381 **Discussion**

382 Here, we elucidate the structure of the T4P^{Mx} using cryo-EM at a resolution of 3.0 Å and

383 demonstrate that, in contrast with all previous T4P structures, the T4P^{Mx} structure is highly

384 compact. The PL of T4P^{Mx} is ~2-fold higher than those of *P. aeruginosa* and *N. gonorrhoeae*,

385 consistent with the greatly increased contacts at higher radius in the T4P^{Mx}. Similarly, the spring

386 constants of T4P^{Mx} at low and moderate pulling speeds are at least 2-fold higher than those

387 reported for *P. aeruginosa* T4P, indicating a greater axial stiffness of T4P^{Mx}. Also, T4P^{Mx} can

388 resist pulling forces up to 400-500 pN, in agreement with the observation that T4P^{Mx} can resist

389 forces up to 150pN generated during retractions[7]. These data make the T4P^{Mx} the strongest and

390 most rigid T4P yet described. Nevertheless, T4P^{Mx} have elastic properties and undergo a force-

391 induced elongation in response to pulling forces as previously described for T4P of *N.*

392 *gonorrhoeae, N. meningitidis,* and *P. aeruginosa*[28-31].

393 The T4P^{Mx} is more compact, more rigid, and stronger than other T4P due to the larger

394 globular domains, which are involved in more extensive intermolecular interactions than seen in

395 other T4P structures. The larger C-terminal globular domains provide surfaces for extensive

396 interactions, causing a measurable increase in total interface area, and allow every individual

397 pilin to interact with six pilins above and six below. Among these six interfaces, the three largest

398 are the N:N-3, N:N-4, and N:N-1, and all three interfaces contain residues that engage in

399 intersubunit salt bridges, i.e. R30$_N$ and/or K37$_N$ and E53$_{N-3}$ in N:N-3, R73$_N$ and/or R109$_N$ and

400 D55$_{N-4}$ in N:N-4, and E69$_N$ and K48$_{N-1}$, R70$_N$ and E175$_{N-1}$ in N:N-1 (Fig. 5A-C). Disruption of

401 these three subunit interfaces reduced the bending stiffness of the corresponding T4P^{Mx}

402 variants but the disruption of the salt bridge connecting two globular domains in the N:N-4

403 interface had the strongest effect, supporting the hypothesis that the large globular domains

404 contribute significantly to the increased bending stiffness.

405 We also observed that the PilA variants K37Q/A, E53Q/A, R70Q/A, R73Q/A had

406 reduced stability (Fig. 5D, E), suggesting that these residues are important for intramolecular

407 interactions before the incorporation of PilA into the T4P and that mutagenesis of these residues

408 causes misfolding and degradation of PilA*. This is similar to earlier findings, showing that

409 mutagenesis of A18, I19 and A20 of PilA^{Mx} (I19 and A20 are part of the melted region, Fig. 3A,

410 B) can strongly affect PilA accumulation[52,53]. Interestingly, mutagenesis of other major pilins also

411 support the notion that intra- and intersubunit salt bridges contribute to the stability of the pilin,

412 assembly of the T4P, and T4P function[21,23,25,54-56].

413   T4P-dependent motility was stimulated by increased substrate stiffness. A similar

414   observation was made in *P. aeruginosa,* and it was suggested that this stimulation involves an

415   increased probability of T4P retraction on the stiffer agar surface[51]. Interestingly, the PilA

416   variants in which subunit interfaces were disrupted supported T4P extension as efficiently as

417   native PilA. However, the T4P made from these PilA variants were less efficient at supporting

418   T4P-dependent motility than PilA[WT] at all substrate stiffnesses. The T4P made from the PilA

419   variants had a reduced PL, indicating decreased bending stiffness or flexural rigidity. However,

420   the PL did not correlate with the ability to support motility suggesting that it is not the decreased

421   bending stiffness *per se* that results in the motility defect. Also, even variant T4P with PLs

422   similar to those of T4P of *P. aeruginosa* and *N. gonorrhoeae* did not support motility. During the

423   extension/adhesion/retraction cycles, only retractions generate a force sufficient to pull a cell

424   forward[5,6], suggesting that the variant T4P likely have retraction defects. The hexameric PilB

425   and PilT ATPases that power extension and retraction, respectively, bind at the base of the

426   T4PM in a mutually exclusive manner[10]. The swap from PilB to PilT, and thus initiation of

427   retraction, was suggested to be a stochastic event[57], or, alternatively, it was suggested that it is

428   induced by adhesion of the pilus tip to the substratum in a process in which tip adhesion causes

429   conformational changes in the pilus that are communicated to the base of the T4PM[58]. *N.*

430   *gonorrhoeae* and *P. aeruginosa* T4P, as also reported here for T4P[Mx], undergo force-induced

431   conformational changes to elongate[28-30]. Therefore, we speculate that the motility defect of the

432   T4P variants could be caused by (1) less efficient transmission of conformational changes from

433   the tip to the base of the T4PM to stimulate the swap from PilB to PilT, (2) reduced ability to

434   undergo force-induced conformational changes during retraction, or (3) even breakage of the

435   T4P when it is pulled taut during retraction.

436   Our results advance our understanding of how sequence divergence of major pilins shapes the

437   functional properties of T4P. Moreover, the information gained from the first complete T4P

438   model, composed of major pilins, four minor pilins, and a large PilY1 adhesin, provides insights

439   into the interactions between major and minor pilins, as well as between minor pilins and

440   PilY1.In future studies of T4P, it will not only be interesting to obtain the structure of T4P formed

441   by large major pilins from different bacteria to further reveal their ecological relevance but also

442   to obtain detailed insights into the interactions between the tip complex and the remaining T4P.

443

15

444   **Methods**

445   Bioinformatics. Sequences of the K02650 (type IV pilus assembly protein PilA) were extracted

446   from the KEGG SSDB database[59]. To filter out highly homologous sequences we used the cdhit

447   program with a threshold of 90% sequence identity[60]. The 2308 obtained sequences were

448   analyzed for presence of T3SP and subsequently processed into the mature pilin form using

449   SignalP (6.0)[61]. The taxonomic classification of the remaining 2071 pilin sequences was

450   collected from KEGG SSDB database and sequences without a bacterial classification as well

451   as sequences from bacterial phyla, only represented by one genome, were excluded from the

452   analysis. The 1955 remaining pilin sequences were analyzed with the PROMALS3D multiple

453   sequence and structure alignment server[62] to obtain aa and secondary structure consensus

454   sequences on the base of the previously solved T4P structures.

455   Alignments were generated using T-Coffee[63] and the ClustalW output format[64]. They were

456   shaded using the BoxShade Server or the BioEdit sequence alignment editor (7.2.5)[65]. For the

457   phylogenetic tree, the ANCESCON tool[66] of the MPI bioinformatics Toolkit[67] was used. The

458   phylogenetic tree was annotated using iTol (v6)[68].

459   Bacterial strains, plasmids and growth media. Strains and plasmids are listed in Supplementary

460   Tables 3 and 4, respectively. All *M. xanthus* strains are derivatives of the DK1622 WT strain[50].

461   In-frame deletion mutants were generated as described[69]. All plasmids were verified by

462   sequencing. All strains were confirmed by PCR and sequencing. Oligonucleotides are listed in

463   Supplementary Table 5. *M. xanthus* strains were grown at 32°C in 1% casitone broth (CTT) (1%

464   casitone, 10mM Tris-HCl pH 8.0, 1mM KPO_4 pH 7.6, 8mM $MgSO_4$) or on 1% CTT, 1.5% agar

465   plates supplemented with kanamycin (40µg ml^{-1}) when required[70]. Growth was followed by

466   measuring optical density at 550nm (OD_{550}). *E. coli* strains were grown in lysogeny broth (LB)[71].

467   Plasmids were propagated in *E. coli* Mach1.

468   T4P purification and T4P shearing assays. T4P were sheared off from the hyper-piliated Δ*pilT*

469   strain using a protocol based on the procedure of[72]. Briefly, cells grown on 1% CTT, 1.5% agar

470   plates for 2-3 days were gently scraped off the agar and resuspended in 4 ml/plate pili

471   resuspension buffer (100mM Tris-HCl pH 7.6, 150mM NaCl). The pooled suspension was

472   centrifuged for 20 min at 13,000 *g* at 4°C to remove cell debris. The supernatant was

473   centrifuged twice for 10 min at 13,000 *g* at 4°C. T4P in the cell-free supernatant were

474   precipitated by adding 10× pili precipitation buffer (final concentrations: 100mM $MgCl_2$, 500mM

475   NaCl, 2% PEG 6000) for at least 2 hrs at 4°C. The solution was centrifuged for 30 min at 13,000

476   *g* at 4°C, and the pellet resuspended 1ml pili resuspension buffer. The pili solution was loaded

16

477   on top of a centrifuge tube containing a 10-70% sucrose gradient (29 ml) of pili resuspension

478   buffer. After 15 hrs centrifugation at 115,000xg in a swing bucket rotor (SW72Ti) at 4°C, the

479   tube was punched at the bottom, and 1.5 ml fractions harvested and analyzed by SDS-PAGE

480   using SDS-lysis buffer (10% (v/v) glycerol, 50mM Tris-HCl pH 6.8, 2mM EDTA, 2% (w/v) SDS,

481   100mM DTT, 0.01% bromphenol blue). To remove the sucrose, PilA-containing fractions were

482   diluted 13.5 fold in pili resuspension buffer, and the solutions precipitated again with pili

483   precipitation buffer (s.a.). The pili were resuspended in pili resuspension buffer.

484   For T4P shearing assays, 60 mg cells grown on 1% CTT, 1.5% agar plates for 2-3 days were

485   gently scraped off the agar and resuspended in pili resuspension buffer. Cell suspensions were

486   vortexed for 10 min at the highest speed. Cells from a 100 µl aliquot were harvested, the pellet

487   solved in 100 µl SDS lysis buffer, and immediately denatured at 95°C for 5 min. This represents

488   the cellular fraction. The remaining suspension was centrifuged for 20 min at 13,000 g at 4°C.

489   The supernatant was removed and centrifuged twice for 10 min at 13,000 g at 4°C to remove

490   cell debris. T4P in the cell-free supernatant was precipitated by adding 10× pili precipitation

491   buffer for at least 2 hrs at 4°C. The solution was centrifuged for 30 min at 13,000 g at 4°C, and

492   the pellet was resuspended in SDS lysis buffer (1µl per mg vortexed cells). T4P sheared and

493   purified from the same amount of cells were loaded and separated by SDS-PAGE.

494   Transmission electron microscopy. Resuspended solutions of sheared T4P were applied on 300

495   mesh Formvar/carbon copper-grids. After 10 min, grids were washed twice with water and

496   negative-staining was done with a solution based on an Organotungsten compound (Nano-W,

497   Nanoprobes). Grids were inspected with a JEM-1400 electron microscope (JEOL) at 100 kV.

498   *Cryo-EM sample preparation and data collection.* 2 µl of a T4P^{Mx} sample was applied to plasma-

499   cleaned lacey carbon grids, followed by plunge-freezing in liquid ethane using a Leica EM GP.

500   Data collection was carried out at liquid nitrogen temperature on a Titan Krios microscope

501   (Thermo Fisher Scientific) operated at an accelerating voltage of 300 kV. Using a K3 camera

502   (Gatan), 40 movie frames were collected with a total dose of ~55 electron/Å^2 and sampling of

503   1.08Å/pixel. The movies were collected with defocus values ranging between -1 to -2.5 µm.

504   Cryo-EM image processing and reconstruction. All the subsequent data processing was

505   performed in CryoSPARC. Raw movie frames were used in the motion correction, followed by

506   CTF estimation. Images with poor CTF estimation were eliminated. Filament tracer was used for

507   filament picking and a total of 6,155,222 256 px-long segments were extracted from 13,006

508   CTF-corrected images. After final round of 2D classification, 1,312,119 segment remained and

17

509   was subjected to homogenous refinement, which yield a map of recognizable secondary

510   structure features when imposing the 1-start helical symmetry. The helical parameters

511   converged to a twist of 100.7° and a rise of 10Å per subunit. The resolution of the final

512   reconstruction was determined by two-independent half maps showing a resolution of 3.0Å at

513   FSC=0.143.

514   <u>Model building and refinement</u>. An initial homologous model generated via SWISS-MODEL was

515   docked into the cryo-EM map by rigid body fitting in Chimera[73] and manually edited the model in

516   Coot[74]. The modified monomeric model was then real-space refined using Phenix[75] to improve

517   the stereochemistry as well as the model-map correlation coefficient. The refined monomeric

518   model was re-built by RosettaCM with helical symmetry, followed by another three rounds of

519   real-space refinement to reduce subunit clashes. The refined symmetrical model was validated

520   with MolProbity[76], and the coordinates were deposited to the Protein Data Bank with the

521   accession code 8TJ2. The corresponding cryo-EM map was deposited in the EMDB with

522   accession code EMD-41298.

523   <u>AlphaFold-Multimer model building.</u> Structures were predicted using AlphaFold-Multimer

524   modeling via ColabFold (Version 1.5.0)[77-79]. The predicted Local Distance Difference Test

525   (pLDDT) and predicted Alignment Error (pAE) graphs of the five models generated were made

526   using a custom Matlab R2020a (The MathWorks) script[80]. Per residue model accuracy was

527   estimated based on pLDDT values (>90, high accuracy; 70-90, generally good accuracy; 50-70,

528   low accuracy; <50, should not be interpreted)[78]. Relative domain positions were validated by

529   pAE. The pAE graphs indicate the expected position error at residue X if the predicted and true

530   structures were aligned on residue Y; the lower the pAE value, the higher the accuracy of the

531   relative position of residue pairs and, consequently, the relative position of

532   domains/subunits/proteins[78]. PyMOL version 2.4.1 (Schrödinger LLC) was used to analyze and

533   visualize the models. Structure superposition of the top PilA of the T4P[Mx] with the bottom PilA of

534   the AlphaFold-Multimer model was done using the align function in PyMol (root mean square

535   deviation=0.841). The protein sequences of the mature minor pilins and PilY1 proteins without

536   their signal peptides as reported earlier[11], were used for generating the models.

537   <u>Determination of subunit interface areas.</u> The interfacial areas were determined by PDBePISA

538   (https://www.ebi.ac.uk/pdbe/pisa/)[81].

539   <u>Persistence length determination</u>. To determine the flexibility of different T4P, persistence length

540   measurements were performed using micrographs of negatively stained T4P from indicated

541 strains. For each strain 30-50 filaments were traced using the ImageJ analysis tool[82].

542 Persistence length (L) is determined by the statistical relationship of cos (θ) and contour length

543 (λ), according to exp(-λ/L)=<cos(θ)>.

544 <u>AFM tip functionalization and FS.</u> Gold AFM probes (PNP-TR, NanoWorld) were incubated

545 overnight in a 1mM ethanolic 1-dodecanethiol solution to modify them with methyl groups and

546 render them hydrophobic, then rinsed with ethanol and sterile water and kept in milliQ water at

547 4°C until use (no longer than 48 hrs). Early exponential-phase *M. xanthus* cultures (OD_{550} ~ 0.5)

548 grown in CTT at 32°C in the dark, were diluted in MC7 buffer (10 mM MOPS pH 7.6, 1 mM

549 $CaCl_{2)}$ and passaged gently through a 26 gauge needle to dissolve cell aggregates before

550 seeding cells in a 35mm untreated polystyrene Petri dish (Corning). After 30 min incubation to

551 allow cells to adhere, they were adequately adhering for high-quality AFM-FS, gently rinsed with

552 MC7 buffer and immediately used for AFM. Prior to any AFM measurements, the spring

553 constant of the probe's cantilever was determined as reported previously[83] allowing for the

554 accurate correlation between measured cantilever deflection with tensile force in stretched T4P.

555 AFM recordings were done at room temperature using a NanoWizard® 4 NanoScience AFM

556 (JPK Instruments) in force mapping (volume) mode, which allows the recording of *F-d* curves in

557 a pixel-by-pixel fashion over a defined surface area in a raster array. Sample height could be

558 determined from the approach section of each *F-d* curve, while the retract portion provided pilus

559 forced extension and adhesive information and hence correlated images of sample topography

560 and pilus mechanical properties allowing mapping of pilus signatures with respect to the cell

561 body. For each tip-cell pair, a large (10×10 μm, 32 × 32 pixels) force map was first recorded to

562 generate a topographical image of a whole cell and to find pilus signatures. Subsequently, a

563 smaller (3×3 μm, 32×32 or 16×32 pixels) map was recorded over a piliated pole. Cells were

564 visualized using an inverted microscope prior to commencement of AFM force mapping. *F-d*

565 curve analysis was performed using the JPK data processing software. The nanospring

566 constant (given as k_{pilus} below) was calculated using the serial spring equation: $\frac{1}{k_{eff}} = \frac{1}{k_{pilus}} + \frac{1}{k_s}$,

567 with k_{eff} (effective spring constant) equal to the slope of the linear region of a nanospring

568 extension profile in an *F-d* curve and k_s (spring constant of the cantilever sensor). Graphs

569 pertaining to AFM data was generated using R Studio.

570 <u>T4P-dependent motility assays.</u> Cells from exponentially growing *M. xanthus* cultures were

571 harvested and resuspended in 1% CTT to a calculated density of 7×10^9 cells ml^{-1}. 5μl of cell

572 suspension were spotted on soft agar CTT plates (0.5% casitone, 10mM Tris-HCl pH 8.0, 1mM

573 KPO_4 pH 7.6, 8mM $MgSO_4$, with the indicated concentrations of select agar (Invitrogen)) and

19

574 incubated at 32°C for 24 hrs. Colony edges were imaged using a Leica MZ75 stereomicroscope

575 with a Leica MC120 HD camera.

576 <u>Antibodies and immunoblot analysis.</u> Immunoblotting was done with rabbit, polyclonal α-PilA

577 and α-LonD antibodies[11]. As secondary antibodies goat, anti-rabbit immunoglobulin G

578 peroxidase conjugate (Sigma-Aldrich, A8275) was used. Blots were developed using

579 Luminata™ Western HRP substrate (Millipore).

580 <u>Data availability.</u> The authors declare that all data supporting this study are available within the

581 article, the Supplementary Information file or are available from the corresponding authors upon

582 request. The source data underlying Fig. 1A, B; 2F; 5D, E, F; S2E, H; S4A; S5 are provided as

583 a Source Data file.

584

References

585 **References**

586 1   Wadhwa, N. & Berg, H. C. Bacterial motility: machinery and mechanisms. *Nat Rev Microbiol* **20**,
587   161-173, (2022).

588 2   Miyata, M. *et al.* Tree of motility - A proposed history of motility systems in the tree of life. *Genes*
589   *Cells* **25**, 6-21, (2020).

590 3   Craig, L., Forest, K. T. & Maier, B. Type IV pili: dynamics, biophysics and functional
591   consequences. *Nat. Rev. Microbiol.* **17**, 429-440, (2019).

592 4   Giltner, C. L., Nguyen, Y. & Burrows, L. L. Type IV pilin proteins: versatile molecular modules.
593   *Microbiol. Mol. Biol. Rev.* **76**, 740-772, (2012).

594 5   Merz, A. J., So, M. & Sheetz, M. P. Pilus retraction powers bacterial twitching motility. *Nature*
595   **407**, 98-102, (2000).

596 6   Skerker, J. M. & Berg, H. C. Direct observation of extension and retraction of type IV pili. *Proc*
597   *Natl Acad Sci U S A* **98**, 6901-6904, (2001).

598 7   Clausen, M., Jakovljevic, V., Søgaard-Andersen, L. & Maier, B. High-force generation is a
599   conserved property of type IV pilus systems. *J Bacteriol* **191**, 4633-4638, (2009).

600 8   Maier, B., Potter, L., So, M., Seifert, H. S. & Sheetz, M. P. Single pilus motor forces exceed 100
601   pN. *Proc Natl Acad Sci U S A* **99**, 16012-16017, (2002).

602 9   Gold, V. A., Salzer, R., Averhoff, B. & Kuhlbrandt, W. Structure of a type IV pilus machinery in the
603   open and closed state. *elife* **4**, e07380, (2015).

604 10   Chang, Y. W. *et al.* Architecture of the type IVa pilus machine. *Science* **351**, aad2001, (2016).

605 11   Treuner-Lange, A. *et al.* PilY1 and minor pilins form a complex priming the type IVa pilus in
606   *Myxococcus xanthus. Nat Commun* **11**, 5054, (2020).

607 12   Bischof, L. F., Friedrich, C., Harms, A., Søgaard-Andersen, L. & van der Does, C. The type IV
608   pilus assembly ATPase PilB of *Myxococcus xanthus* interacts with the inner membrane platform
609   protein PilC and the nucleotide-binding protein PilM. *J Biol Chem* **291**, 6946-6957, (2016).

610 13   Craig, L., Pique, M. E. & Tainer, J. A. Type IV pilus structure and bacterial pathogenicity. *Nat Rev*
611   *Microbiol* **2**, 363-378, (2004).

612 14   Herfurth, M. *et al.* A noncanonical cytochrome c stimulates calcium binding by PilY1 for type IVa
613   pili formation. *Proc Natl Acad Sci U S A* **119**, (2022).

614 15   Xue, S. *et al.* The differential expression of PilY1 proteins by the HsfBA phosphorelay allows
615   twitching motility in the absence of exopolysaccharides. *PLoS Genet* **18**, e1010188, (2022).

616 16   Rudel, T., Scheurerpflug, I. & Meyer, T. F. *Neisseria* PilC protein identified as type-4 pilus tip-
617   located adhesin. *Nature* **373**, 357-359, (1995).

618 17   Strom, M. S., Nunn, D. N. & Lory, S. A single bifunctional enzyme, PilD, catalyzes cleavage and
619   N-methylation of proteins belonging to the type IV pilin family. *Proc Natl Acad Sci U S A* **90**, 2404-
620   2408, (1993).

621   18   Sheppard, D. *et al.* The major subunit of widespread competence pili exhibits a novel and
622   conserved type IV pilin fold. *J Biol Chem* **295**, 6594-6604, (2020).

623   19   Gu, Y. *et al.* Structure of *Geobacter* pili reveals secretory rather than nanowire behaviour. *Nature*
624   **597**, 430-434, (2021).

625   20   Wang, F., Craig, L., Liu, X., Rensing, C. & Egelman, E. H. Microbial nanowires: type IV pili or
626   cytochrome filaments? *Trends Microbiol* **31**, 384-392, (2023).

627   21   Wang, F. *et al.* Cryoelectron microscopy reconstructions of the *Pseudomonas aeruginosa* and
628   *Neisseria gonorrhoeae* type IV pili at sub-nanometer resolution. *Structure* **25**, 1423-1435 e1424,
629   (2017).

630   22   Kolappan, S. *et al.* Structure of the *Neisseria meningitidis* type IV pilus. *Nat Commun* **7**, 13015,
631   (2016).

632   23   Bardiaux, B. *et al.* Structure and assembly of the enterohemorrhagic *Escherichia coli* type 4 pilus.
633   *Structure* **27**, 1082-1093 e1085, (2019).

634   24   Wang, F. *et al.* Cryo-EM structure of an extracellular *Geobacter* OmcE cytochrome filament
635   reveals tetrahaem packing. *Nat Microbiol* **7**, 1291-1300, (2022).

636   25   Lopez-Castilla, A. *et al.* Structure of the calcium-dependent type 2 secretion pseudopilus. *Nat*
637   *Microbiol* **2**, 1686-1695, (2017).

638   26   Neuhaus, A. *et al.* Cryo-electron microscopy reveals two distinct type IV pili assembled by the
639   same bacterium. *Nat Commun* **11**, 2231, (2020).

640   27   Craig, L. *et al.* Type IV pilus structure by cryo-electron microscopy and crystallography:
641   implications for pilus assembly and functions. *Mol Cell* **23**, 651-662, (2006).

642   28   Touhami, A., Jericho, M. H., Boyd, J. M. & Beveridge, T. J. Nanoscale characterization and
643   determination of adhesion forces of *Pseudomonas aeruginosa* pili by using atomic force
644   microscopy. *J Bacteriol* **188**, 370-377, (2006).

645   29   Biais, N., Higashi, D. L., Brujic, J., So, M. & Sheetz, M. P. Force-dependent polymorphism in type
646   IV pili reveals hidden epitopes. *Proc Natl Acad Sci U S A* **107**, 11358-11363, (2010).

647   30   Beaussart, A. *et al.* Nanoscale adhesion forces of *Pseudomonas aeruginosa* type IV pili. *ACS*
648   *Nano* **8**, 10723-10733, (2014).

649   31   Brissac, T., Mikaty, G., Duménil, G., Coureuil, M. & Nassif, X. The meningococcal minor pilin PilX
650   is responsible for type IV pilus conformational changes associated with signaling to endothelial
651   cells. *Infect Immun* **80**, 3297-3306, (2012).

652   32   Wu, S. S. & Kaiser, D. Genetic and functional evidence that Type IV pili are required for social
653   gliding motility in *Myxococcus xanthus*. *Mol Microbiol* **18**, 547-558, (1995).

654   33   Bader, C. D., Panter, F. & Müller, R. In depth natural product discovery - Myxobacterial strains
655   that provided multiple secondary metabolites. *Biotechnol Adv.* **39**, 107480, (2020).

656   34   Konovalova, A., Petters, T. & Søgaard-Andersen, L. Extracellular biology of *Myxococcus xanthus*.
657   *FEMS Microbiol. Rev.* **34**, 89–106, (2010).

658 35 Zhang, Y., Ducret, A., Shaevitz, J. & Mignot, T. From individual cell motility to collective
659   behaviors: insights from a prokaryote, *Myxococcus xanthus. FEMS Microbiol. Rev.* **36**, 149-164,
660   (2012).

661 36 Shi, W. & Zusman, D. R. The two motility systems of *Myxococcus xanthus* show different
662   selective advantages on various surfaces. *Proc Natl Acad Sci U S A* **90**, 3378-3382, (1993).

663 37 Kanehisa, M., Sato, Y., Kawashima, M., Furumichi, M. & Tanabe, M. KEGG as a reference
664   resource for gene and protein annotation. *Nucleic Acids Res* **44**, D457-462, (2016).

665 38 Garrity, G. M., Bell, J. A. & Lilburn, T. in *Bergey's Manual of Systematics of Archaea and Bacteria*
666   (2015).

667 39 Coenye, T. & Vandamme, P. Diversity and significance of *Burkholderia* species occupying
668   diverse ecological niches. *Environ Microbiol* **5**, 719-729, (2003).

669 40 Martinucci, M. *et al.* Accurate identification of members of the *Burkholderia cepacia* complex in
670   cystic fibrosis sputum. *Lett Appl Microbiol* **62**, 221-229, (2016).

671 41 Ligthart, K., Belzer, C., de Vos, W. M. & Tytgat, H. L. P. Bridging bacteria and the gut: Functional
672   aspects of type IV pili. *Trends Microbiol* **28**, 340-348, (2020).

673 42 Rozman, V., Accetto, T., Duncan, S. H., Flint, H. J. & Vodovnik, M. Type IV pili are widespread
674   among non-pathogenic Gram-positive gut bacteria with diverse carbohydrate utilization patterns.
675   *Environ Microbiol* **23**, 1527-1540, (2021).

676 43 Orans, J. *et al.* Crystal structure analysis reveals *Pseudomonas* PilY1 as an essential calcium-
677   dependent regulator of bacterial surface motility. *Proc Natl Acad Sci U S A* **107**, 1065-1070,
678   (2010).

679 44 Remaut, H. & Waksman, G. Protein-protein interaction through beta-strand addition. *Trends
680   Biochem Sci* **31**, 436-444, (2006).

681 45 Vetsch, M. *et al.* Mechanism of fibre assembly through the chaperone-usher pathway. *EMBO Rep*
682   **7**, 734-738, (2006).

683 46 Zyla, D., Echeverria, B. & Glockshuber, R. Donor strand sequence, rather than donor strand
684   orientation, determines the stability and non-equilibrium folding of the type 1 pilus subunit FimA. *J
685   Biol Chem* **295**, 12437-12448, (2020).

686 47 Galkin, V. E., Orlova, A., Vos, M. R., Schroder, G. F. & Egelman, E. H. Near-atomic resolution for
687   one state of f-actin. *Structure* **23**, 173-182, (2015).

688 48 Galkin, V. E., Orlova, A. & Egelman, E. H. Actin filaments as tension sensors. *Current Biology* **22**,
689   R96-R101, (2012).

690 49 Lu, S. *et al.* Nanoscale pulling of type IV pili reveals their flexibility and adhesion to surfaces over
691   extended lengths of the pili. *Biophys J* **108**, 2865-2875, (2015).

692 50 Kaiser, D. Social gliding is correlated with the presence of pili in *Myxococcus xanthus. Proc. Natl.
693   Acad. Sci. USA* **76**, 5952-5956, (1979).

694 51 Cont, A., Vermeil, J. & Persat, A. Material substrate physical properties control *Pseudomonas
695   aeruginosa* biofilm architecture. *mBio*, e0351822, (2023).

696 52 Yang, Z. *et al.* Alanine 32 in PilA is important for PilA stability and type IV pili function in
697   *Myxococcus xanthus. Microbiology (Reading)* **157**, 1920-1928, (2011).

698 53 Yang, Z., Lux, R., Hu, W., Hu, C. & Shi, W. PilA localization affects extracellular polysaccharide
699   production and fruiting body formation in *Myxococcus xanthus. Mol Microbiol* **76**, 1500-1513,
700   (2010).

701 54 Nivaskumar, M. *et al.* Distinct docking and stabilization steps of the Pseudopilus conformational
702   transition path suggest rotational assembly of type IV pilus-like fibers. *Structure* **22**, 685-696,
703   (2014).

704 55 Karami, Y. *et al.* Computational and biochemical analysis of type IV pilus dynamics and stability.
705   *Structure* **29**, 1397-1409 e1396, (2021).

706 56 Campos, M., Nilges, M., Cisneros, D. A. & Francetic, O. Detailed structural and assembly model
707   of the type II secretion pilus from sparse data. *Proc Natl Acad Sci U S A* **107**, 13081-13086,
708   (2010).

709 57 Koch, M. D., Fei, C., Wingreen, N. S., Shaevitz, J. W. & Gitai, Z. Competitive binding of
710   independent extension and retraction motors explains the quantitative dynamics of type IV pili.
711   *Proc Natl Acad Sci U S A* **118**, (2021).

712 58 Tala, L., Fineberg, A., Kukura, P. & Persat, A. *Pseudomonas aeruginosa* orchestrates twitching
713   motility by sequential control of type IV pili movements. *Nat Microbiol* **4**, 774-780, (2019).

714 59 Aoki, K. F. & Kanehisa, M. Using the KEGG database resource. *Curr. Protoc. Bioinformatics* **11**,
715   1.12.11-11.12.54, (2005).

716 60 Li, W. & Godzik, A. Cd-hit: a fast program for clustering and comparing large sets of protein or
717   nucleotide sequences. *Bioinformatics* **22**, 1658-1659, (2006).

718 61 Teufel, F. *et al.* SignalP 6.0 predicts all five types of signal peptides using protein language
719   models. *Nat Biotechnol* **40**, 1023-1025, (2022).

720 62 Pei, J., Tang, M. & Grishin, N. V. PROMALS3D web server for accurate multiple protein
721   sequence and structure alignments. *Nucleic Acids Res* **36**, W30-34, (2008).

722 63 Notredame, C., Higgins, D. G. & Heringa, J. T-Coffee: A novel method for fast and accurate
723   multiple sequence alignment. *J. Mol. Biol.* **302**, 205-217, (2000).

724 64 Thompson, J. D., Higgins, D. G. & Gibson, T. J. CLUSTAL W: improving the sensitivity of
725   progressive multiple sequence alignment through sequence weighting, position-specific gap
726   penalties and weight matrix choice. *Nucleic Acids Res.* **22**, 4673-4680, (1994).

727 65 Hall, T. A. BioEdit: A user-friendly biological sequence alignment editor and analysis program for
728   Windows 95/98/NT. *Nucleic Acids Symposium Series* **41**, 95-98, (1999).

729 66 Cai, W., Pei, J. & Grishin, N. V. Reconstruction of ancestral protein sequences and its
730   applications. *BMC Evol Biol* **4**, 33, (2004).

731 67 Gabler, F. *et al.* Protein sequence analysis using the MPI Bioinformatics Toolkit. *Curr Protoc
732   Bioinformatics* **72**, e108, (2020).

733 68 Letunic, I. & Bork, P. Interactive Tree Of Life (iTOL): an online tool for phylogenetic tree display
734   and annotation. *Bioinformatics* **23**, 127-128, (2007).

735 69 Shi, X. *et al.* Bioinformatics and experimental analysis of proteins of two-component systems in
736   *Myxococcus xanthus. J. Bacteriol.* **190**, 613-624, (2008).

737 70 Søgaard-Andersen, L., Slack, F. J., Kimsey, H. & Kaiser, D. Intercellular C-signaling in
738   *Myxococcus xanthus* involves a branched signal transduction pathway. *Genes Dev.* **10**, 740-754,
739   (1996).

740 71 Sambrook, J. & Russell, D. W. *Molecular cloning : a laboratory manual.* 3rd edn, (Cold Spring
741   Harbor Laboratory Press, 2001).

742 72 Wu, S. S., Wu, J. & Kaiser, D. The *Myxococcus xanthus pilT* locus is required for social gliding
743   motility although pili are still produced. *Mol. Microbiol.* **23**, 109-121, (1997).

744 73 Pettersen, E. F. *et al.* UCSF Chimera--a visualization system for exploratory research and
745   analysis. *J Comput Chem* **25**, 1605-1612, (2004).

746 74 Emsley, P., Lohkamp, B., Scott, W. G. & Cowtan, K. Features and development of Coot. *Acta
747   Crystallogr D Biol Crystallogr* **66**, 486-501, (2010).

748 75 Adams, P. D. *et al.* PHENIX: a comprehensive Python-based system for macromolecular
749   structure solution. *Acta Crystallogr D Biol Crystallogr* **66**, 213-221, (2010).

750 76 Chen, V. B. *et al.* MolProbity: all-atom structure validation for macromolecular crystallography.
751   *Acta Crystallogr D Biol Crystallogr* **66**, 12-21, (2010).

752 77 Evans, R. *et al.* Protein complex prediction with AlphaFold-Multimer. *bioRxiv*,
753   10.1101/2021.1110.1104.463034., (2022).

754 78 Jumper, J. *et al.* Highly accurate protein structure prediction with AlphaFold. *Nature* **596**, 583-
755   589, (2021).

756 79 Mirdita, M. *et al.* ColabFold: making protein folding accessible to all. *Nat Methods* **19**, 679-682,
757   (2022).

758 80 Schwabe, J., Pérez-Burgos, M., Herfurth, M., Glatter, T. & Søgaard-Andersen, L. Evidence for a
759   widespread third system for bacterial polysaccharide export across the outer membrane
760   comprising a composite OPX/beta-barrel translocon. *mBio* **13**, e0203222, (2022).

761 81 Krissinel, E. & Henrick, K. Inference of macromolecular assemblies from crystalline state. *J Mol
762   Biol* **372**, 774-797, (2007).

763 82 Collins, T. J. ImageJ for microscopy. *Biotechniques* **43**, 25-30, (2007).

764 83 Hutter, J. L. & Bechhoefer, J. Calibration of atomic-force microscope tips. *Review of Scientific
765   Instruments* **64**, 1868-1873, (1993).

766

773

774 **Authors' contributions**:

775 ATL: Designed and conceived the study, analyzed the length and phylogenetic distribution of T4

776 pilins (K02650), purified T4P, constructed and characterized *M. xanthus* strains expressing

777 PilA^{Mx} variants, and determined PL for T4P from PilA^{Mx} variants. WZ: Performed the cryo-EM

778 data collection, image processing and reconstruction, model building and refinement, and

779 determined PL for T4P from Mx, Ng and Pa. AV: Performed the AFM force spectroscopy

780 analyses and analyzed the data. SL: Generated plasmids and strains and performed motility

781 assays. MH: Generated the AlphaFold-Multimer models and helped with the KEGG group

782 sequence aquisition. YFD: Supervised AFM force spectroscopy and provided funding. LSA:

783 Conceived the study, supervised research and provided funding. EHE: Conceived the study,

784 supervised research and provided funding. ATL, LSA and EHE: Analyzed and interpreted data

785 and wrote the manuscript. All authors approved the final manuscript.

786

787 **Competing interests**: The authors declare no competing interests.

788

Figure 1. Length and phylogenetic distribution of major pilins

A. The length distribution of major pilins of the KEGG orthology group K02650 (type IV pilus assembly protein PilA) in the complete dataset of 1,955 sequences (light blue, all) grouped according to taxonomy at the phylum (light green) and class level (light yellow); the "other" category (light grey) includes sequences from phyla/classes with <2% of all 1,955 sequences and in which major pilins are not enriched. Grey dots, major pilins ≤165 aa; purple dots, large major pilins (≥166 aa), and blue dots, major pilins of solved T4P of the K02650 group (PilE from *N. meningitidis* (Nm PilE; 5KUA)[22]; PilA from *P. aeruginosa* PAK (Pa PilA; 5VXY)[21]; PilE from *N. gonorrhoeae* (Ng PilE; 5VXX)[21]; PilA4 from *T. thermophilus* (Tt PilA4; 6XXD)[26]; PilA-N from *G. sulfurreducens* (Gs PilA-N; 6VK9)[19]). Error bars, mean length ± standard deviation (STDEV). Black numbers (n) above the x-axis, total number of sequences in a phylum/class. Purple numbers (n), number of large major pilins, and their % of the total number in a phylum/class. Please note that PpdD from enterohemorrhagic *E. coli* (Ec PpdD; 6GV9)[23], PulG from *K. oxytoca* (Ko PulG; 5WDA)[25] and PilA5 from *T. thermophilus* (Tt PilA5; 6XXE)[26] are not depicted. PpdD belongs to K02682 (prepilin peptidase dependent protein D), which is composed of
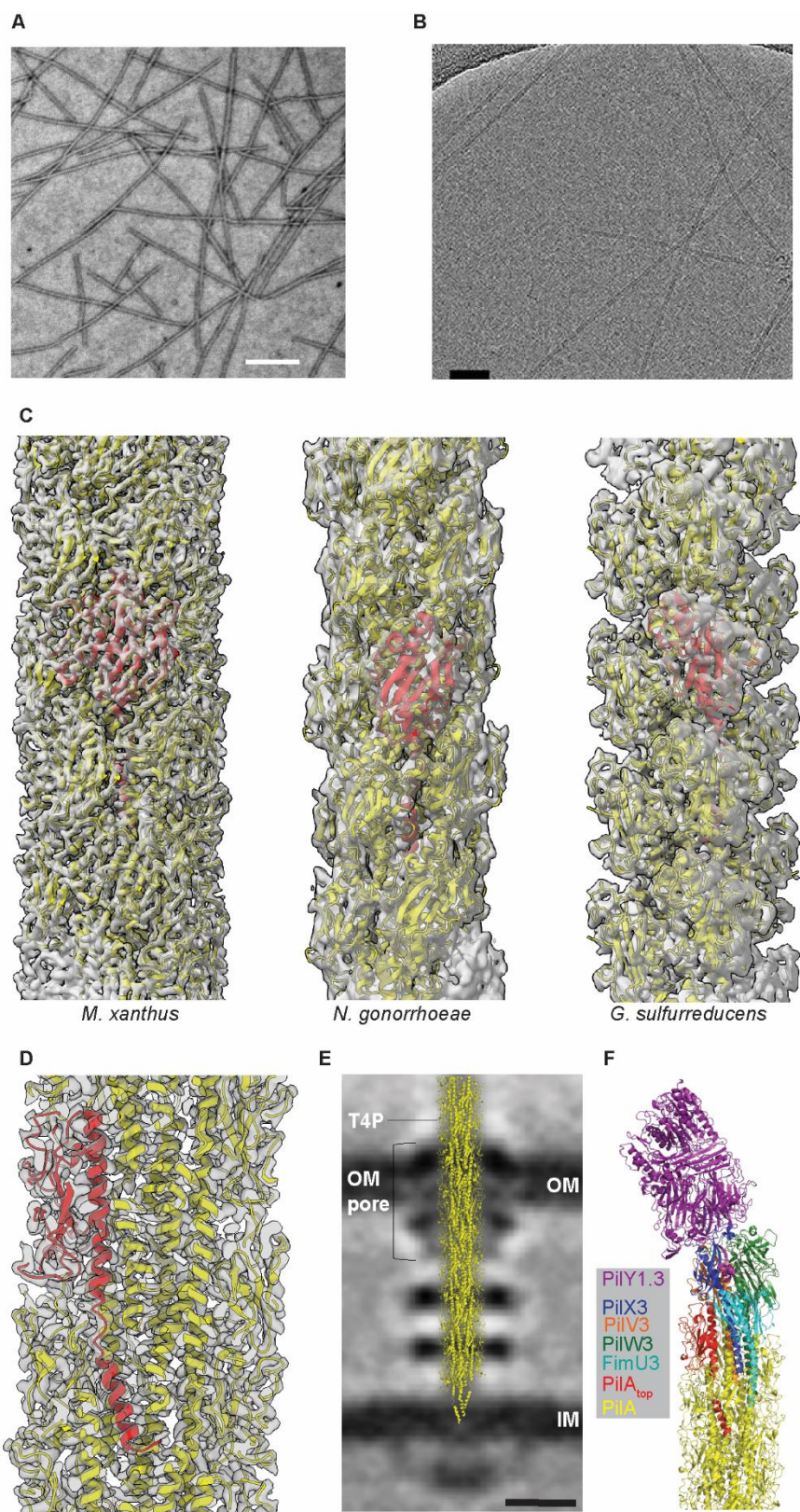
27

806   predominantly enterobacterial PpdD homologous sequences with a full length <150aa, PulG

807   belongs to K02456 (GspG, general secretion pathway protein G) and PilA5 is not yet assigned

808   to a KEGG group.

809   **B.** Consensus sequence (con. aa) and consensus secondary structure (con. ss-α) of α1-helix

810   based on 1,955 mature major pilin sequences and major pilins of previously solved T4P

811   structures. The sequences comprising the α1-helix of major pilins of the solved T4P structures

812   as in **A** are included for comparison. For comparison, the sequence comprising the α1-helix of

813   PilA from *M. xanthus* (Mx PilA) is also included[11].

814   **C.** Schematic of overall architecture of major pilins of solved T4P structures. Red boxes, α1-N

815   and α1-C, with the melted stretch in-between in light red. Numbers, total length of the α1-helix,

816   and the end as well as start of α1-N and α1-C. The sequences used are as in **A**. Note that the

817   major pilin of G. *sulfurreducens* is heterodimeric and composed of PilA-N (61 aa) and PilA-C

818   (104 aa)[19].

819

A

B

C

M. xanthus

N. gonorrhoeae

G. sulfurreducens

D

E

T4P

OM
pore

OM

IM

F

PilY1.3
PilX3
PilV3
PilW3
FimU3
PilA_top
PilA

820

821

822 **Figure 2. Cryo-EM structure of the T4P^Mx.**

29

823   **A.** Representative micrograph of negatively stained T4P^{Mx}. Scale bar, 200nm.

824   **B.** Representative cryo-EM micrograph of T4P^{Mx}. Scale bar, 500nm.

825   **C.** Comparison of cryo-EM reconstructions of T4P and ribbon models of pilins from *M. xanthus*

826   (left), *N. gonorrhoeae* (center), and the 2-chain G. *sulfurreducens* (right), where the transparent

827   surfaces are the cryo-EM density maps, and one pilin subunit is shown in red in each.

828   **D.** Cross section of the cryo-EM reconstruction of the T4P^{Mx} with a single PilA subunit shown in

829   red.

830   **E**. Placement of the T4P^{Mx} structure into the central slice of the subtomogram average of the

831   piliated *M. xanthus* T4PM revealed by cryo-electron tomography[10]. The T4P, the outer

832   membrane pore (OM pore), OM, and IM are indicated. Scale bar, 10nm.

833   **F.** Complete T4P^{Mx} structure composed of T4P^{Mx} and a tip complex. The top PilA of the T4P^{Mx} is

834   shown in red and PilA subunits of T4P^{Mx} below are shown in yellow, the AlphaFold-Multimer

835   model containing the four minor pilins (FimU3, PilV3, PilW3, PilX3) and PilY1.3 is shown in the

836   indicated colors. The complete T4P^{Mx} structure was generated by superposing the top PilA (red)

837   of the T4P^{Mx} with the bottom PilA (wheat) of the AlphaFold-Multimer model (RMSD=0.841,

838   Fig.S2E). The superposed PilA from the AlphaFold-Multimer model is not shown in the complete

839   T4P^{Mx} structure.

840

841

842
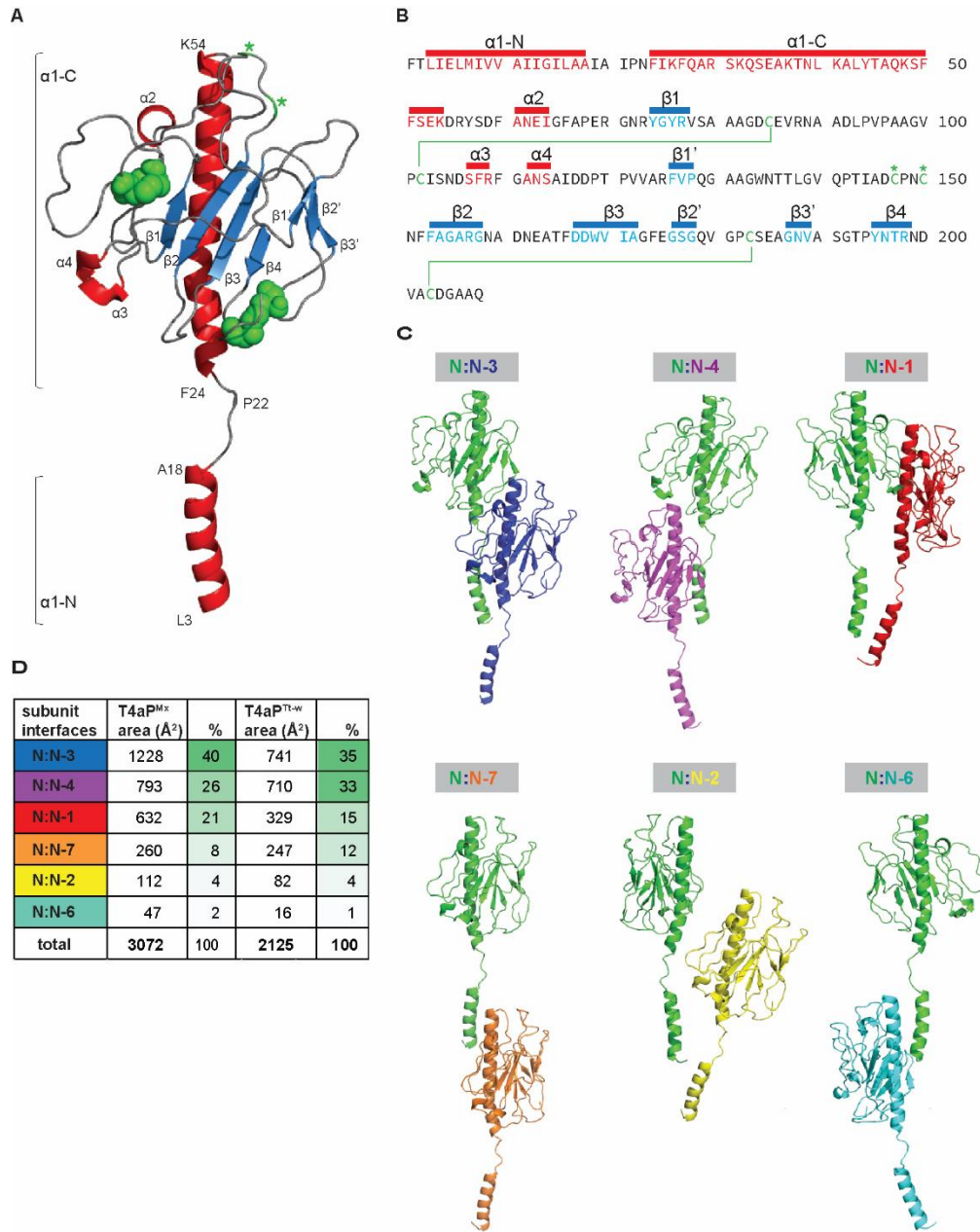
Figure 3. Atomic model of PilA^Mx and subunit interface analysis within the T4P^Mx filament.

A. Ribbon representation of PilA^Mx, with helical elements (α1-4) shown in red, β-stranded elements (β 1-4, β1'-3') shown in blue, less-structured areas in grey, disulfide bridges shown in green and free cysteines shown with green stars. The first and last residues of the helices of α1-N and α1-C are shown as well as the localization of the conserved Pro 22 within the melted region.

B. Sequence of PilA depicting structural elements, disulfide bridges, and free cysteines as in **A.**

850   **C.** Ribbon representation of the six different subunit interfaces with the largest three on top and

851   the three smaller ones at the bottom. The color code of the subunits is shown above.

852   **D.** Areas of the six different subunit interfaces of T4P^{Mx} in comparison to the interfaces in the

853   wide T4P of *T. thermophilus* and percentage of those different areas of the total sum shown with

854   a green to white color scale. The color code of the subunit interface corresponds to the subunit

855   interacting with N as in **C**.

856
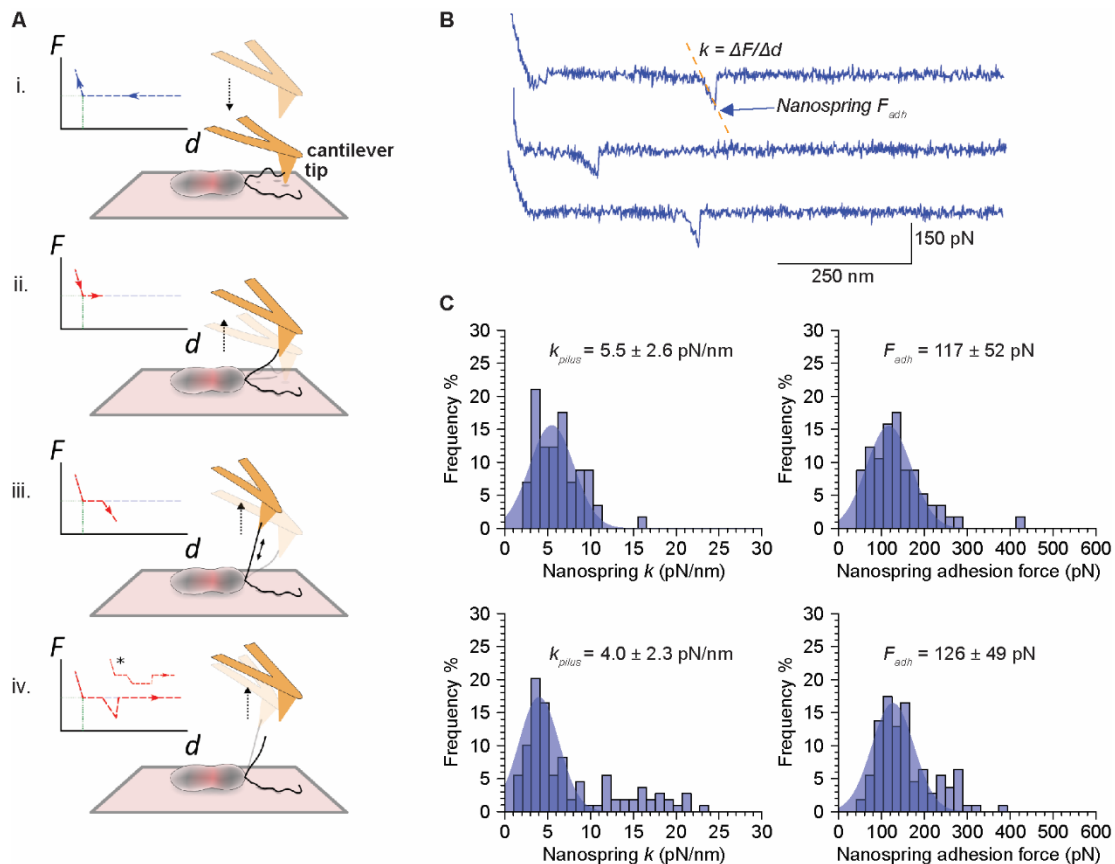
Figure 4. T4P^{Mx} have increased axial stiffness and elastic properties and undergo force-induced elongation in response to pulling forces by AFM-FS.

A. Schematic of AFM-FS approach to collect force-extension profiles of *M. xanthus* T4P. (i) Cells in buffer were adhered to a polystyrene surface. The hydrophobic AFM probe on the cantilever approached towards the surface near one of the cell poles until it touches and pushes on the surface of the dish or cell, causing the upwards bending of the cantilever that is recorded as a positive force in the approach Force-distance (*F-d*) curve (blue). By chance, a T4P freely floating in the buffer adheres to the hydrophobic tip (i.e. hydrophobic contacts are established between the solvent accessible surface of the pilus fiber and the CH_3 groups exposed on the AFM tip). (ii) The AFM tip is retracted away from the surface lifting the relaxed T4P until (iii) the T4P becomes loaded with tension resulting in downwards bending of the cantilever, thereby allowing quantification of the tensile force (red *F-d* curve). (iv) When the tensile force within the T4P exceeds that of the bonds between the pilus and the hydrophobic AFM tip, the contact between the two is ruptured and the cantilever relaxes resulting in a zero-force measurement (baseline) in the *F-d* curve. Two types of signatures are expected for T4P, linear (Hookean) nanosprings and constant force plateaus (indicated with an asterisk in the *F-d* curve).

33

875   **B.** Three representative *F-d* curves obtained for WT *M. xanthus* cell showing nanospring

876   signatures. The rupture/adhesion force (F_{adh}) is indicated by a blue arrow, the dotted line

877   indicates the slope of the nanospring profile used to determine its spring constant (k_{pilus}).

878   **C.** Histograms showing the distribution of nanosprings k_{pilus} (left) and F_{adh} (right) as determined

879   from *F-d* curves generated at a probe retraction velocity of 1µm/sec (top, n= 57 nanosprings in

880   82/1312 curves from 5 tip-cell combinations) or 5µm/sec (bottom, n= 109 nanosprings in

881   44/5400 curves from 5 tip-cell combinations). Numbers indicate mean ± STDEV.

882

884
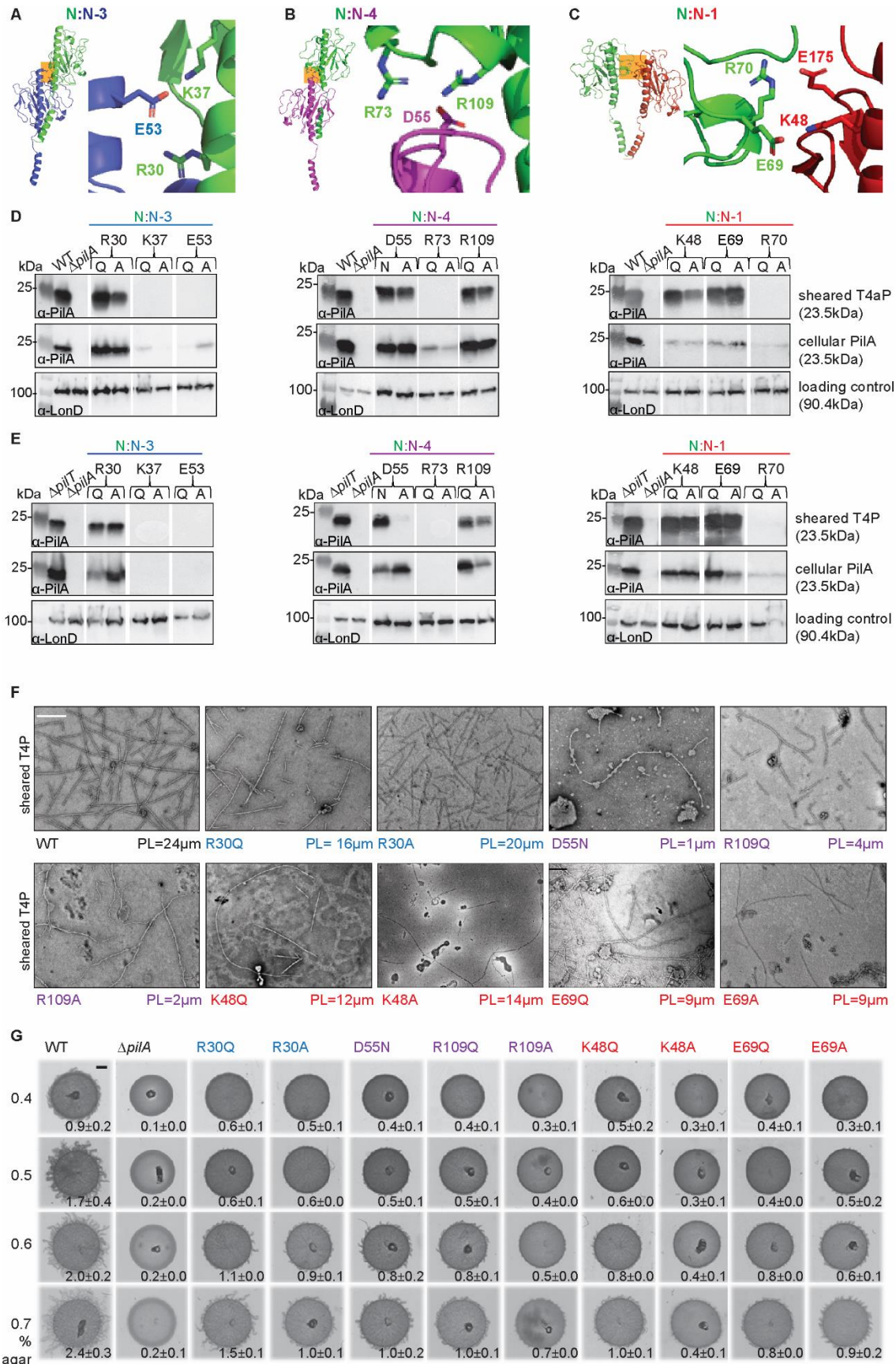
Figure 5. Mutagenesis of selected charged residues in PilA subunit interfaces.

A-C. Ribbon representation of interacting subunits N:N-3 (A), N:N-4 (B) and N:N-1 (C) as overviews (left parts) with orange boxes indicating the position of the magnified views (right parts) depicting the charged residues in these areas. The depicted residues, except for E175, were all targeted for mutagenesis. The subunit color code is as in Fig. 3C.

D-E. Effect of amino acid substitutions on PilA* accumulation and T4P formation. T4P sheared off from the surface of cells (top rows), and total cell extracts (middle rows) were separated by SDS-PAGE and probed with α-PilA antibodies. The membrane used for cell extracts was stripped, and probed with α-LonD antibodies as a loading control (bottom rows). Material from the same amount of cells was loaded per lane. The PilA variants were analyzed in WT (**D**) and the Δ*pilT* mutant (**E**). Proteins with their calculated molecular masses and positions of molecular markers are indicated. Gaps between lanes indicate lanes that were deleted for presentation purposes.

F. Negative staining micrographs of sheared T4P. PL values in μm are shown below the images. Scale bar, 250 nm. Note that these pili, in contrast to those in Fig. 2A, were imaged directly after the precipitation and not further purified by sucrose gradient centrifugation.

G. Substitutions at intersubunit interfaces perturb T4P-dependent motility. Cells were incubated 24 hrs before imaging. The Δ*pilA* mutant served as a negative control. Scale bar, 1 mm. Numbers indicate mean±STDEV of increase in colony diameter in 24hrs from two independent experiments.

905

906